

DelTact: A Vision-based Tactile Sensor Using Dense Color Pattern

Guanlan Zhang, Yipai Du, Hongyu Yu and Michael Yu Wang, *Fellow, IEEE*

Abstract—Tactile sensing is an essential perception for robots to complete dexterous tasks. As a promising tactile sensing technique, vision-based tactile sensors have been developed to improve robot manipulation performance. Here we propose a new design of our vision-based tactile sensor, DelTact, with its high-resolution sensing abilities of multiple modality surface contact information. The sensor adopts an improved dense random color pattern based on previous version, using a modular hardware architecture to achieve higher accuracy of contact deformation tracking whilst at the same time maintaining a compact and robust overall design. In particular, we optimized the color pattern generation process and selected the appropriate pattern for coordinating with a dense optical flow in a real-world experimental sensory setting using varied contact objects. A dense tactile flow was obtained from the raw image in order to determine shape and force distribution on the contact surface. This sensor can be easily integrated with a parallel gripper where experimental results using qualitative and quantitative analysis demonstrated that the sensor is capable of providing tactile measurements with high temporal and spatial resolution.

I. INTRODUCTION

Through millennia of evolutionary processes, humans have been evolved a tactile sense of touch as a critical sensory method of interaction with objects. Delicate tasks, including tactile perception, grasping different shaped objects, manipulation of tools, can be completed with fluency and insight with direct sensory feedback. Since then, the ratio between intelligent robots and humans has been increasing worldwide. In many working fields, robotic systems are pursuing more dexterity in the face of contact-rich scenarios, where tactile sensors are being developed to detect the necessary tactile information for robot interaction with objects and environments.

Conventional tactile sensors utilizing transduction components (e.g., piezoresistive, capacitive, and piezoelectric sensors) usually have the common problems of high sensitivity to environmental conditions (such as temperature, fluctuation, and electrical interference) and complicated peripheral electronics when the sensing area is expanded. In recent years, research into vision-based tactile sensors has grown due to superiorities in high resolution, easy fabrication, robustness against environmental change, an ability for multi-axial measurement, and simple multiplexing circuits. Development in digital cameras has made capturing contact situations with high-quality images of low cost and easy to interface with. Moreover, advances in computer vision and

This research work is supported in part by the Innovation and Technology Fund of the Government of the Hong Kong Special Administrative Region (Project No. ITS-104-19FP).

G. Zhang, Y. Du, H. Yu and M. Y. Wang are with the Hong Kong University of Science and Technology, Hong Kong (e-mail: {gzhangaq, yduaz}@connect.ust.hk, {hongyuuyu, mywang}@ust.hk).

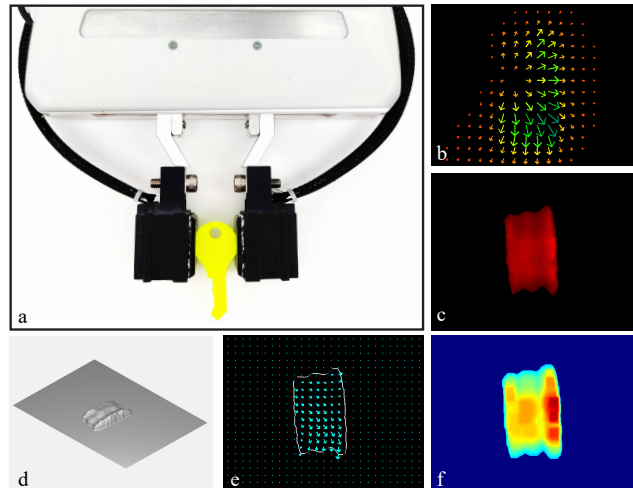


Fig. 1. a) Two DelTact sensors are mounted on a FE Gripper of PANDA Robotic Arm to grasp a yellow key. b) Visualized optical flow. c) Gaussian density plotted in hot map. d) Isometric view of the shape reconstruction. e) Estimated shear force distribution. f) Estimated normal force distribution.

deep learning assist in transferring knowledge from visual perception to tactile perception, enabling faster analysis of high dimensional tactile representation in larger images.

In this paper, we present DelTact, a new version of the vision-based tactile sensor based on our previous framework [1]. The sensor is designed to be compact and convenient in integrating itself into modern robotic systems such as grippers and robot fingers using online sensing of shape and force in high spatial and temporal resolution. Our work thus makes three main contributions to this field:

- Presenting a modular hardware design and simplified manufacturing process for a new tactile sensor making consideration to durability, compactness, and ease of assembly.
- Proposing a parametric optimization framework of the previous random color pattern [2] with indentation experiment to track 2D displacement field at higher accuracy.
- Integrating online tactile measurement algorithms into software to extract 3D shape and force information at a high spatial and temporal resolution.

The paper proceeds as follows: Section. II introduces the previous vision-based tactile sensor designs and tactile information processing. Section. III shows problems in our past sensors and principles for the new design. In Section. IV, we give a complete description of design and fabrication of the proposed sensor. In Section. V, tactile measurement algorithm and experiment results are presented. Finally, in Section. VI, discussion and conclusion with future research identified.

II. RELATED WORK

A. Vision-based Tactile Sensor

Early development of vision-based tactile sensor can be traced back to Kamiyama et al. [3], where colored markers were deployed in transparent elastomer and tracked by a CCD camera to measure the gel deformation at different depths. This prototype later was developed into GelForce [4], which could obtain complete information on contact force (i.e., direction, magnitude and distribution).

Continued research based on the GelForce-type working principle focused on a more compact form factor hardware with broadened functionalities of the sensor to better integrate with robotic systems such as robot hands and grippers. Yamaguchi et al. [5], [6] proposed a fingervision sensor to combine visual and tactile sensing with only one monocular camera. Nathan et al. [7], [8] introduced the TacTip family with a bio-inspired data acquisition system to simulate mechanoreceptors under human skin and detect contact information. Sferrazza et al. [9], [10] presented a full-resolution optical tactile sensor using random distributed green markers to achieve high-accuracy force sensing. Kuppuswamy et al. [11] showed a Soft-bubble gripper with a pseudorandom dot pattern to estimate shear deformation. These sensors are all characterized by simple structures and easy fabrication, but face the problem of low spatial resolution in feature recognition and interpretation.

Another series of GelSight-type sensor adopts a retro-graphic sensing technique to obtain high-resolution 3D deformation. Representative work here with GelSight, was by Yuan et al. [12], [13], who cast colored light onto Lambertian reflectance skin to measure the surface normal of deformation directly, and reconstructed the dense accurate 3D shape. To further reduce the size of the sensor for convenient installation onto grippers, GelSlim [14], [15] was developed with optimized optical and hardware design. Padmanabha et al. [16] demonstrated a finger-size touch sensor, OmniTact to perform multi-directional tactile sensing. Lambeta et al. [17] released their fingertip Digit sensor with integrated circuit design at low cost for extensive application in robot manipulation. However, GelSight-type sensors require uniformity in both diffuse albedo and illumination, which increases the difficulty in terms of optical design incorporating with system. Also, each sensor needs to calibrate the relationship between surface normal and image color intensity.

B. Tactile Information Extraction

The origin signal received by the vision-based tactile sensors contains diverse compound information, which is dependent on the contact condition between sensor and environment. Furthermore, to achieve dexterity in challenging tactile-related tasks such as tactile exploration, grasping, manipulation, and locomotion, more than one perceptive measurement is required for control. Therefore, tactile information extraction algorithms generally have capacity in multi-modality measuring of contact and versatility in recognizing various levels of features with multiple models [18].

Tactile sensors directly obtain low-level features such as deformation [5], texture [13], contact area localization [14], geometry reconstruction [12] and force estimation [9], [12] at the contact site. Algorithms with low complexity can solve the problem using linear regression [13], principal component analysis (PCA) [19], and graphic features such as entropy [20], Voronoi feature [21] and Gaussian density [2]. Besides, complicated tasks that require high-level information have been performed smartly, including object recognition [22], localization of dynamic object [23], simultaneous localization and mapping on objects [24], slip detection [25] and a fine-grained contact events classification [26]. Such works usually require larger amount of data and more complex models to describe and control. Learning-based methods are preferred to analyze high-dimensional raw images with good generalization and accuracy. In our work, we aim at using cost-effective algorithms to estimate low-level contact shape and force distribution as a proof of concept for our tactile sensing method.

III. PROBLEMS AND DESIGN PRINCIPLES

In the previous tactile sensors that we developed, a dense random color pattern sticker was attached to a soft transparent elastomer and captured by a monocular camera to obtain the deformation of the contact surface. The pattern's inner side is directly illuminated by white LEDs and a silver color paint layer is coated on the outside to block the environmental light influences [2]. This particular design makes the surface deformation more obvious to track and demands less restriction on light source compared to GelSight-type sensors, which require an almost even distribution of three color lights and a Lambertian reflectance skin [13]. Also, the sensor can be redesigned into various shapes with similar configurations such as a robot arm [1] or a robot foot [27] to provide tactile measurement in different systems.

However, several drawbacks were found that impact the sensor performance and reliability during usage. First, a stable imaging condition is required where only the surface deformation is captured by the camera, and it was found that the previous sensor structure was not entirely isolated from the environment. Although a 3D printed shell blocks most external influences, two assembly holes on the shell let light, dust, and tinny objects enter, which disturbs the displacement tracking. Besides, limited by the focal length of the camera, the dimension of the sensor, especially height, which is prescribed with a minimum to obtain desired field of view (FOV) for sensing area. This limit makes the sensor bulky and restricts further integration with grippers or robot fingers. Moreover, the sensor is fabricated as an entirety without replaceable or repairable components except for the camera module. Once any part of the sensor is damaged, the whole device is inoperable and must be replaced. In particular, the silver color paint layer takes hours to cure and detaches from the elastomer under extreme shear load. The failure of this layer is the leading cause of sensor failures.

To solve the above problems, we propose the following design principles to improve the previous tactile sensor.

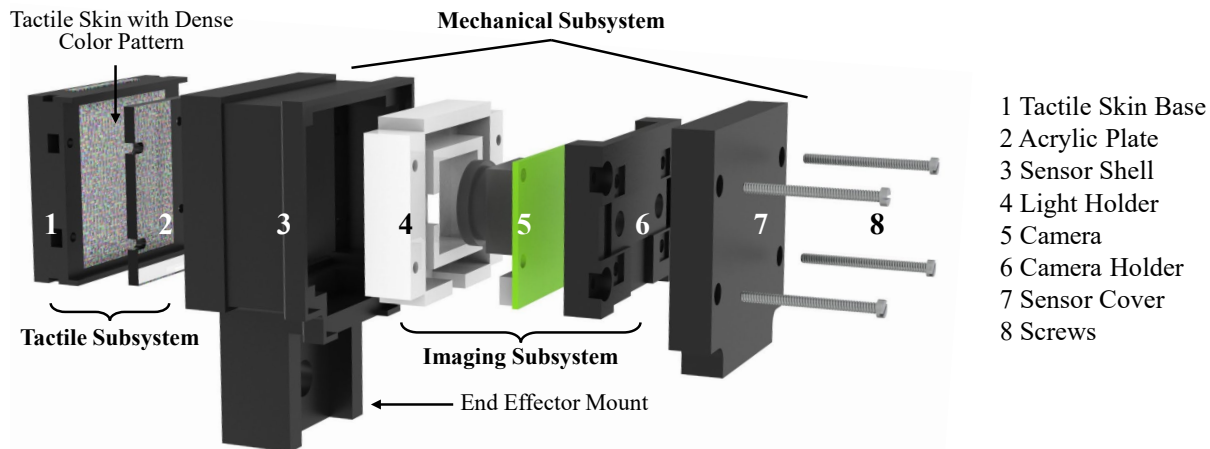


Fig. 2. Mechanical configuration of DelTact (explosive view).

- 1) **Robustness:** The sensor should provide accurate and stable tactile performance. This requires higher mechanical strength for longer service life and fewer noises during image capturing. The simpler fabrication process also reduces manufacturing fault rate.
- 2) **Compactness:** With a small compact size, the sensor is enabled for better integration with robot fingers to perform manipulation tasks under different scenarios while avoiding collision with environmental objects.
- 3) **Easy to Use:** A modular structural design is fabricated to make the sensor easy to assemble and replace. Electrical parts including signal and power are also convenient for connection.
- 4) **Multi-modality Measurement:** Rich contact information such as force distribution, shape, surface point cloud with high resolution and accuracy is extracted online using computation-effective algorithms. These features can be utilized in control systems for accomplishing various tactile-related tasks.

IV. SENSOR DESIGN AND FABRICATION

In this section, we give a detailed description of the design of DelTact. Based on the aforementioned design principles, improvements are implemented in different aspects including, system configuration (IV-A), dense color pattern (Section IV-B) and fabrication processes (Section IV-C).

A. System Configuration

The system configuration of DelTact consists of three subsystems (i.e., the tactile subsystem, imaging subsystem, and mechanical subsystem) underlying the primary function of the sensor. The subsystems can be further disassembled into eight individual parts. Each part is designed for the least space required to achieve as much compactness as possible. Details about the subsystems are presented below.

1) *Tactile Subsystem:* The tactile subsystem comprises a tactile skin base and an acrylic plate. The tactile skin base is a black housing frame that fixes the tactile skin with dense color pattern at the bottom. It avoids skin detachment from the sensor and eliminates undesired reflection for imaging.

For the tactile skin material, we choose a transparent soft silicone rubber (Solaris™ from Smooth-On, Inc.). The Solaris™ satisfies our requirement for both softness and toughness with a shore hardness of 15A and tensile strength of 180 psi. The thickness of the tactile skin is 12 millimeters and a sensing area of 36mm×34mm is obtained with fillets on edges to reduce wear. To guarantee enough support against excessive deformation under external load, a 2-mm thick rectangle acrylic plate is attached tightly to the back of the skin.

2) *Imaging Subsystem:* The imaging subsystem consists of a light holder and a camera module. The light holder is made of semitransparent white resin, and a light strip with five 5050 SMD LEDs inserted into the holder. The strip is powered by a 5-volt direct current passing through a series resistance of 750 ohms for current-limiting protection. Owing to the inner reflection of the light holder, light from LEDs is homogenized and cast more uniformly on the tactile sensing surface.

For the camera, we choose the Waveshare IMX219 Camera Module with a short fisheye lens to achieve a 200-degree FOV and close minimum photographic distance. This camera is well consistent with our compact design principle and acquires images with a higher resolution of 1280 × 720 at 60 frames per second. Regarding signal transmission, the camera is connected to an Nvidia Jetson Nano B01 board, where the image can be directly processed on board or sent to another host PC through ROS communication. To integrate the camera into the system, a camera holder is inserted to lock the camera with two M2 screws, preventing vibration and protecting its circuit.

3) *Mechanical Subsystem:* The mechanical subsystem includes the sensor shell and the sensor cover. The purpose of designing the shell and the cover is to encapsulate the tactile sensing parts from outside interference and achieve maximum compact assembly. Therefore, the shell and cover are opaque and fully enclose the sensor to block external light and dust. The wall thickness of these components is 1.5 millimeters to ensure sufficient strength. Concerning flexible assembly and reducing relative slip, the cover has four snap-fit cylinders connected to the camera holder.

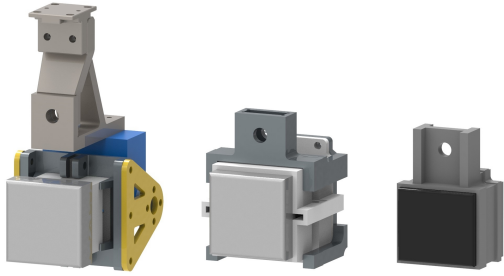


Fig. 3. 3D model of previous Gecko-enhanced tactile sensor (left), FingerVision sensor (middle) and DelTact (right).

All the sensor components are assembled firmly by four 19-mm long M1.6 screws, and each part can be replaced for maintenance within minutes thanks to the modular design. We design a 20-mm long end effector mounted on the shell to work with the FE gripper of a Panda robotic arm (shown in Fig. 1.a). The geometry and the mount’s position can be easily remodeled to fit into different grippers. The overall dimension of the sensor is $39 \times 60 \times 30 \text{ mm}^3$ with the end effector mount counted in. As shown in Fig. 3, the size of DelTact is significantly reduced compared to the previous sensors [2][28], while the sensing area is almost maintained the same.

B. Dense Color Pattern Optimization

Optical flow tracking of dense random color pattern is the prime algorithm that we utilize to measure surface deformation. The vector field obtained from the algorithm represents the 2D projection of the 3D surface deformation on camera frame, from which rich contact information can be extracted. Thus, tracking accuracy of the pattern influences the sensor performance at a fundamental level. Here we propose improvements of optical flow with adaptive referencing which has been proposed in [2] and is briefly reviewed in Section IV-B.1. Then, we mainly focus on generating color patterns with high randomness (Section IV-B.2) and selection of color pattern to achieve more accurate tracking results (Section IV-B.3).

1) *Dense Optical Flow and Adaptive Referencing*: We pursue a dense optical flow using Gunnar Farneback’s algorithm [29] benefiting from a more efficient computation. The algorithm infers a deformation vector field from the image sequence at a higher frequency on GPU. The algorithm solves the traditional optical flow problem in a dense (per pixel) manner, by finding a warping vector $\mathbf{u} = (u, v)$ for each template patch T in the reference image which minimizes the squared error between patches in reference image and query image I_t .

$$\mathbf{u} = \operatorname{argmin}_{\mathbf{u}'} \sum_x [I_t(\mathbf{x} + \mathbf{u}') - T(\mathbf{x})]^2 \quad (1)$$

where $\mathbf{x} = (x, y)^T$ represents pixels in patch T from the reference image.

While referring to a static initial frame causes imperfections under large deformation when the rigid template matching fails to track the distorted pattern, an adaptive referencing strategy can be introduced to automatically select

a new reference frame during operation. An inverse wrapped image is computed based on a coarser flow and compared with current image. Once the photometric error between two images exceeds a fixed threshold, the current image is set to replace the old reference image for tracking. During this process, the total optical flow is the superposition of all the flow calculated. This method guarantees that a matched correspondence between each frame is accurate and allows small non-linear transformation for the template image [2].

2) *Pattern Generating*: The purpose of using a dense color pattern is that the dense optical flow algorithm estimates the motion of patches based on their value variance as shown in Eq. 1. Therefore, an initial frame where every pixel has distinct RGB (or grayscale) values contains more features to track as opposed to a monochromatic image that is untrackable.

Four parameters, i.e., height h , width w , patch size d , and randomness regulation factor r , are predetermined to form the pattern. Width and length prescribe the resolution of the pattern. Here the patch size determines the length of the square color patch in mm. For instance, as the pattern is printed in an area of $35 \times 35 \text{ mm}^2$, a resolution of 350×350 and patch size of 0.2 indicate that each color patch is $0.2 \times 0.2 \text{ mm}^2$ and takes up 2×2 pixels.

Algorithm 1 Patch Generating

Input:

- Patch size in pixels, d ;
- Randomness regulation factor between neighbors, r ;
- List of neighbor patches, L ;

Output:

- Dense color patch, P ;
 - 1: Initialize zero value matrix P with shape $d \times d \times 3$;
 - 2: **for** each patch P_i in L **do**
 - 3: Store RGB values R_i, G_i, B_i of P_i ;
 - 4: **end for**
 - 5: Generate $R, G, B = \operatorname{rand}(0, 1)$;
 - 6: **while** $\max(|R - R_i|, |G - G_i|, |B - B_i|) < r$ **do**
 - 7: Regenerate R, G, B ;
 - 8: **end while**
 - 9: Apply R, G, B to RGB channels of P ;
 - 10: **return** P
-

To generate the color pattern, we began with filling the first patch at the top-left of the image. We selected three numbers randomly from 0 to 1 and applied the values to its RGB channels. Then the rest of the patches were computed based on the existing patches. A neighbor patch of a particular patch was defined if it contacted with an edge or vertices of that patch. Moreover, we used the randomness regulation factor, $r \in [0, 1)$ to adjust the variance of RGB values between neighbor patches. A new patch was filled so that the minimum value difference in each RGB channel between the new patch and its neighbors was larger than r . A detailed description of this process is shown in Algorithm 1. We continued to fill the first row and first column of patches, where the neighbors were the left and the upper patches

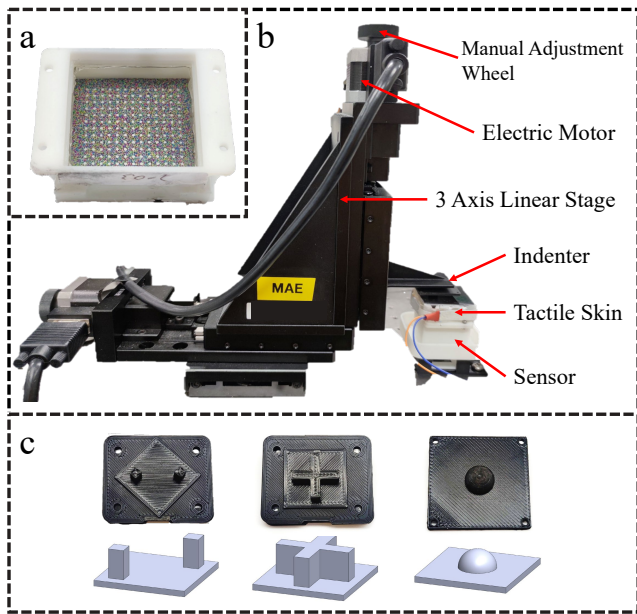


Fig. 4. Pattern selecting experiment configuration. a) Demountable tactile skin base using dense color combined with white dots pattern. For this sample, the patch size $d = 0.2$ mm and the randomness regulation factor $r = 0.3$. b) Data collection with electric 3 axis linear stage. The stage is driven by either an electric motor or a manual adjustment wheel. c) Three types of 3D printed indenters (top) and Solidworks modelings (bottom). From left to right: 2 dots, cross, sphere.

respectively. Finally, all unfilled patches were computed in sequence with row-major order taking into consideration the neighbor patches generated previously.

3) *Pattern Selecting*: Because the ink printing quality and the camera resolution are limited, patterns with minimal patch size and extremely high randomness will influence the imaging process, causing ambiguities in feature recognition. To choose the proper dense color pattern that fits well with the optical flow method, we conducted an indentation experiment to measure the accuracy of flow tracking using different patterns. We fabricated nine tactile skin bases with patch size $d \in \{0.1, 0.15, 0.2\}$ and randomness regulation factor $r \in \{0.1, 0.3, 0.5\}$ (a sample is shown in Fig. 4.a). The skin bases were mounted on a testing sensor that had the same configuration as DelTact but a different shell for fixing on table (shown in Fig. 4.b). Three 3D printed indenters (shown in Fig. 4.c) pressed the sensor surface and moved along x-y-z axis by the electric linear stage to generate surface deformation in all directions.

The experiment is carried out in following steps:

- 1) The sensor with tactile base mounted was fixed on a table.
- 2) The 2 dots indenter was installed on the linear stage.
- 3) The stage was driven to press the sensor surface at four positions, the contact depths at each position were 5 mm and then 10 mm.
- 4) At each depth, the indenter moved in x-y directions for ± 10 mm. During this process, the camera continued to capture the image.
- 5) The stage retracted to its initial position to change the indenter. Then it repeated step 3 to 5.

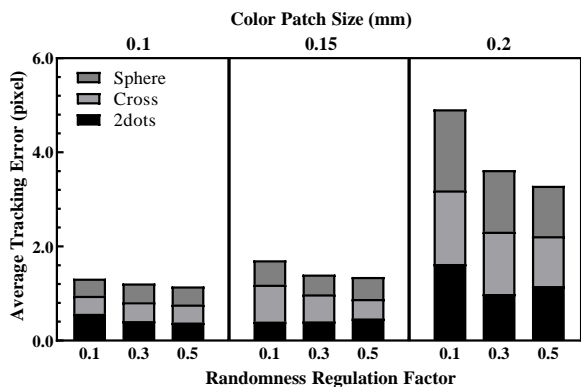


Fig. 5. Compression of the average optical flow tracking error between patterns with different patch size d and random regulation factor r . For each of the nine patterns, three indenters are used and the errors are accumulated.

- 6) After three indenters were used, the tactile base was changed and restarted experiment from step 2.

For each combination of indenter and tactile base, we collected 3600 data points. Each data point was an image with deformed dense color pattern and dots pattern. We used a color filter to separate the white color dots in the image and a blob detection to measure the sub-pixel displacement, $\mathbf{u}_i = (dx_i, dy_i)$, from current position to initial position at $p_i = (x_i, y_i)$ ($i = 1, 2, 3 \dots 169$) for ground truthing. We then ran the dense optical algorithm and calculate the average error δ between the flow displacement vector $\mathbf{u}'_i = (dx'_i, dy'_i)$ at p_i and \mathbf{u}_i . For $n = 169$, the error $\bar{\delta}$ was given by:

$$\bar{\delta} = \frac{\sum_{i=1}^n \sqrt{(x_i - x'_i)^2 + (y_i - y'_i)^2}}{n} \quad (2)$$

The experiment results are shown in the stacked column chart of Fig. 5. The average tracking errors for each pattern under three indenters are accumulated to evaluate the performance under different contact shapes. The pattern with $d = 0.1$ and $r = 0.5$ gives the lowest error of 1.15. Therefore, we proposed using this pattern to fabricate our sensor. We also found that in the experimental range, the tracking error decreases as the patch size and randomness regulation factor increase, which agreed with our initial purpose of using a more random and denser color pattern to obtain more accurate tracking.

C. Fabrication Process

Fabrication of the sensor takes several steps into account. To begin with, for preparation, all the mechanical components and a mold for silicone casting are 3D printed with black or white epoxy resin. Then the solvents of two-part Solaris™ silicone are mixed in a 1 : 1 ratio and rest in a vacuum pump to remove air bubbles. The mixture is poured gently into the mold to cure in desired shape. This mold can cast four modules at a time. Meanwhile, the tactile sensing base is put into the mold to bind together with the tactile skin.

The acrylic plate is laser cut and filmed uniformly with a layer of prime coat (DOWSIL™ PR-1200 RTV from Dow, Inc.) to enhance bonding between the silicone. It is also put

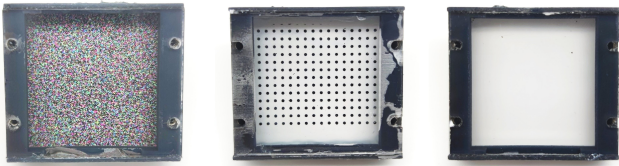


Fig. 6. Tactile sensing skin with three types of pattern (from left to right: dense color pattern, dot matrix, transparent).

onto a tactile sensing base whilst the silicone is curing. The mixed gel cures in 16 hours at room temperature (23°C), and a heating process under 65°C in a constant temperature cabinet can effectively reduce this time to 8-10 hours. When formed, an elastomer layer adheres firmly under the acrylic plate and serves as the deformation interfacing substrate.

The dense color pattern is printed on a ductile soft film sticker. The surface of the sticker becomes adhesive after contacting water and retains smoothness after drying. Thus, the sticker can be easily applied to the elastomer by using a wet brush. We can make different types of pattern stickers for specific data extraction purposes (shown in Fig. 6). When the sticker is dried, two thin layers of protection silicone (Dragon Skin™ 10 FAST from Smooth-On, Inc.) are coated on the pattern. White pigment is added to the inner layer to enhance imaging brightness and disperse light from the LEDs. Compared to the past design of spraying a frosted paint layer [1], this method is simpler but more durable and takes less time to achieve the same effect. The outermost layer is sealed with black pigment to isolate potential external light disturbance and block background interference.

Finally, all eight components are assembled. Due to the minimum tolerance remaining in structural design, the four holes on each part are well aligned for screw threading. And two completed DelTact sensors are mounted onto the FE gripper of Panda robotic arm for testing (shown in Fig. 1.a).

V. TACTILE MEASUREMENT ALGORITHM

In this section, we present the algorithm pipeline for extracting tactile information, i.e., shape and contact force, from the image. The experiments results of tactile measurements are presented in demonstrating sensor performance.

A. Image Preprocessing

As we used a fisheye lens to obtain a large FOV and fully cover the sensing area, the camera required calibration to the correct radial and tangential distortion. In addition, distortion also occurs due to the thick silicone layer which adds a lens effect to the original image. Therefore, we took this into account by calibrating the camera module for the influence of the gel.

We adopted calibration method as introduced in the OpenCV camera calibration tutorial [30]. To capture the distorted image through silicone, we fabricated a tactile base with solely a transparent Solaris™ layer (the right one shown in Fig. 6) and mounted it onto the sensor. A chessboard (shown in Fig. 7.3) was printed to mark the 3D position of points in world frame w.r.t. the camera. The calibration process took 14 pictures with different rotation angle around

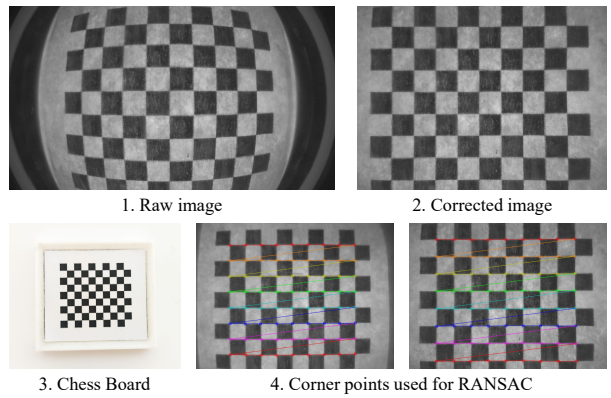


Fig. 7. Image preprocessing. 1. Raw image taken by camera through transparent silicone. 2. Corrected image with intrinsic parameters. The image is resized and cropped into a resolution of 798 × 586. 3. Printed chessboard. Each black area on the board is a 4 × 4 mm² square. 4. Highlighted corner points used for RANSAC. The distance between the parallel board and the camera frame in real world is 12 mm in the first image and 10 mm in the second image.

the x-y-z axis as input (shown in Fig. 7.1). It returned intrinsic parameters of a camera matrix and a distortion coefficients matrix for OpenCV undistortion function. The corrected image was resized and cropped to obtain the ROI (shown in Fig. 7.2) for optical flow calculation. Finally, we used RANSAC method to calibrate extrinsic parameters of rotation and translation vectors corresponding to the camera frame. The RANSAC process used two images parallel to the camera surface at a different distance (shown in Fig. 7.4). The algorithm managed to regress the result within a reprojection error of 6 pixels (0.2mm in real world).

B. Shape Reconstruction

The method of 3D shape reconstruction was presented in our previous work [2] based on the prior optical flow with adaptive referencing mentioned in Section IV-B.1. Because the 2D optical flow is essentially a projection of 3D deformation on camera, an expansion field indicates a deformation in normal direction. Thus, to extract the shift-invariant measurement of expansion, we wrapped the flow vectors with a 2D Gaussian distribution kernel given its covariance matrix

$$\mathbf{Q} = \begin{bmatrix} \sigma^2 & 0 \\ 0 & \sigma^2 \end{bmatrix}. \quad (3)$$

In practice, we set $\sigma = 3.0$, and the relative depth of the surface deformation was directly estimated from negative Gaussian density. A guided filter [31] was used to reduce high-frequency noises and smooth the surface while maintaining shape features such as edges. Then we conducted the shape reconstruction for four objects in Fig. 8. The 3D shape of the contact objects is shown in the results including the features of faces, edges, curves, and corners.

C. Contact Force Estimation

Surface total force (normal force and shear force along x-y directions) can be inferred from the vector field based on natural Helmholtz-Hodge decomposition (NHHD) [32]. The

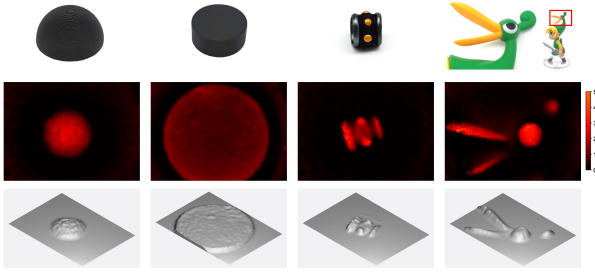


Fig. 8. 3D reconstruction of four shapes (from left to right): sphere, cylinder, ring, and toy hat. The first row are the objects. The second row is the estimated Gaussian densities plotted in hot map. A more reddish region indicates a higher depth. The third row is the isometric view of the deformation.

optical flow \vec{V} is decomposed by

$$\vec{V} = \vec{d} + \vec{r} + \vec{h}, \quad (4)$$

where \vec{d} denotes curl-free component ($\nabla \times \vec{d} = \vec{0}$), \vec{r} denotes divergence-free component ($\nabla \cdot \vec{r} = \vec{0}$), and \vec{h} is harmonic ($\nabla \times \vec{h} = \vec{0}$, $\nabla \cdot \vec{r} = \vec{0}$) [33]. Then summation of vector norms on \vec{d} and norm of vector summation of \vec{V} can be used to estimate total normal force and shear force.

Sometimes a dense distributed force field is preferred in providing richer information for control purposes. To break down total force into force distribution, given the optical flow with NHH components, $\vec{V} = \vec{d} + \vec{r} + \vec{h}$, we first assumed that the magnitude of normal force and shear force $f = [f_{normal} \ f_{shear}]^T$ at the displacement point $p = (i, j)$ followed an n th order polynomial model such that:

$$f = \text{diag}(Ax). \quad (5)$$

A is the polynomial coefficient matrix

$$A = \begin{bmatrix} a_{11} & a_{12} & \dots & a_{1n} \\ a_{21} & a_{22} & \dots & a_{2n} \end{bmatrix}, \quad (6)$$

and x is the polynomial term matrix

$$\begin{bmatrix} D_p & \left\| \vec{h}_p + \vec{r}_p \right\|_2 \\ D_p^2 & \left\| \vec{h}_p + \vec{r}_p \right\|_2^2 \\ \vdots & \vdots \\ D_p^n & \left\| \vec{h}_p + \vec{r}_p \right\|_2^n \end{bmatrix}, \quad (7)$$

where D_p is the processed non-negative Gaussian density, \vec{r}_p is the divergence-free component and \vec{h}_p is the harmonic component at point p . Then A is calibrated by the total force which is assumed to be the superposition of f across the surface. The total force magnitude $F = [F_{normal} \ F_{shear}]^T$ is also defined by the polynomial model as:

$$F = \text{diag}(A), \quad (8)$$

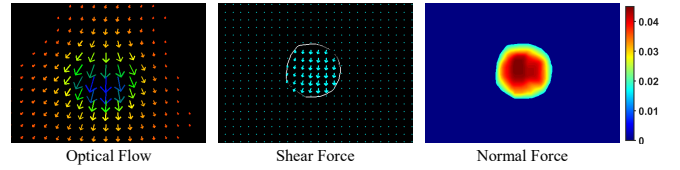


Fig. 9. Force distribution estimation result of a sphere indenter. For visualization, the dense vector field of optical flow and shear force are sparsely displayed. A white contour representing the contact area is shown in the shear force distribution.

with X being

$$\begin{bmatrix} \sum D_p & \left\| \sum (\vec{h}_p + \vec{r}_p) \right\|_2 \\ (\sum D_p)^2 & \left\| \sum (\vec{h}_p + \vec{r}_p) \right\|_2^2 \\ \vdots & \vdots \\ (\sum D_p)^n & \left\| \sum (\vec{h}_p + \vec{r}_p) \right\|_2^n \end{bmatrix}. \quad (9)$$

We collected force and flow data by conducting a similar indentation experiment as shown in Section IV-B. An ATI Nano17 F/T Sensor was installed on the sensor to measure high-accuracy surface normal and shear force. As for the indenters, we used five 3D printed spheres with diameters of 10, 12, 15, 18, and 22 mm. To avoid influence of slip, only steady-state data are recorded. A was solved using linear regression with 4140 data points. We adopted $n = 2$ and the resulting adjusted coefficient of determination R^2 together with root mean square error (RMSE) are shown in Table I.

Force	Adjusted R^2	RMSE (N)
F_{normal}	0.99	0.42
F_{shear}	0.98	0.11

Finally, the calculated model was applied to the sensor where we revealed the force distribution result in Fig. 9. The algorithm achieved an online computation frequency of 30 Hz with an Intel Core i7-6700 CPU and an NVIDIA GTX 1080 GPU.

VI. DISCUSSION AND CONCLUSION

In this work, our previous vision-based tactile sensor [2] was improved using an optimized dense random color pattern for achieving a higher accuracy tactile flow. The proposed sensor, named DelTact, adopts reinforced hardware that features greater compactness and robustness. It can be mounted onto various types of end effectors to carry out robotic tasks. Materials for 3D printed components and the tactile skin were also selected with enhanced durability. The modular structure design and simpler fabrication process enable more convenient use and maintenance. The size of DelTact was reduced by one-third compared to the fingervision sensor whilst keeping the sensory area sufficient for contact measurement. A new camera module captured images of elastomer deformation with a higher resolution of 1280×720 at 60 Hz, which provided rich tactile features for contact information extraction. Random color patterns generated from different parameter sets were tested with

an indentation experiment for minimized tracking error. Regarding software, image preprocessing, shape reconstruction, and contact force estimation algorithms are presented with experimental results showcasing that our sensor has multi-modality sensing abilities with high spatial and temporal resolution.

We acknowledge the compromise between the information quality and limitation of sensor performance, while rough contact feedback can satisfy the system perception demand in some cases with fewer requirements in software, hardware, and indeed prior work. The proposed methods of shape reconstruction with Gaussian density falls short compared with prior works in texture measurement based on photometric stereo such as GelSight [13] and GelSlim [15], which are able to recognize surface features at sub-millimeter scale. However, photometric stereo requires strict conditions for surface reflection and illumination properties. Learning-based force estimation manages to measure contact force within an error of 0.1 N [9], but the confidence of the model prediction relies on a large amount of training data from complex collecting procedures. Therefore, the motivation of our work is to devise an easily fabricated and calibrated sensor that is sufficient and computationally cost-effective in tactile information extraction for a broader range of tasks.

Possible future work includes testing the versatility of the sensor on robot perception and manipulation. Beyond the low-level features, using optical flow, we may try to extract higher-level features such as vibration and slip, which are critical for maintaining stability in grasping tasks. Besides, as Gaussian density introduces noise even with a guided filter, an optimization-based method subject to surface smoothness is considered to obtain higher accuracy 3D point cloud of the tactile skin surface under larger deformation.

REFERENCES

- [1] Y. Zhang, G. Zhang, Y. Du, and M. Y. Wang, "Vtacarm. a vision-based tactile sensing augmented robotic arm with application to human-robot interaction," in *2020 IEEE 16th International Conference on Automation Science and Engineering (CASE)*. IEEE, 2020, pp. 35–42.
- [2] Y. Du, G. Zhang, Y. Zhang, and M. Y. Wang, "High-resolution 3-dimensional contact deformation tracking for fingervision sensor with dense random color pattern," *IEEE Robotics and Automation Letters*, vol. 6, no. 2, pp. 2147–2154, 2021.
- [3] K. Kamiyama, H. Kajimoto, M. Inami, N. Kawakami, and S. Tachi, "A vision-based tactile sensor," in *International Conference on Artificial Reality and Telexistence*, 2001, pp. 127–134.
- [4] K. Vlack, K. Kamiyama, T. Mizota, H. Kajimoto, N. Kawakami, and S. Tachi, "Gelforce: A traction field tactile sensor for rich human-computer interaction," in *IEEE Conference on Robotics and Automation, 2004. TExCRA Technical Exhibition Based*. IEEE, 2004, pp. 11–12.
- [5] A. Yamaguchi and C. G. Atkeson, "Combining finger vision and optical tactile sensing: Reducing and handling errors while cutting vegetables," in *2016 IEEE-RAS 16th International Conference on Humanoid Robots (Humanoids)*. IEEE, 2016, pp. 1045–1051.
- [6] —, "Tactile behaviors with the vision-based tactile sensor fingervision," *International Journal of Humanoid Robotics*, vol. 16, no. 03, p. 1940002, 2019.
- [7] J. W. James, N. Pestell, and N. F. Lepora, "Slip detection with a biomimetic tactile sensor," *IEEE Robotics and Automation Letters*, vol. 3, no. 4, pp. 3340–3346, 2018.
- [8] B. Ward-Cherrier, N. Pestell, L. Cramphorn, B. Winstone, M. E. Giannaccini, J. Rossiter, and N. F. Lepora, "The tactip family: Soft optical tactile sensors with 3d-printed biomimetic morphologies," *Soft robotics*, vol. 5, no. 2, pp. 216–227, 2018.
- [9] C. Sferrazza and R. D'Andrea, "Design, motivation and evaluation of a full-resolution optical tactile sensor," *Sensors*, vol. 19, no. 4, p. 928, 2019.
- [10] C. Trueeb, C. Sferrazza, and R. D'Andrea, "Towards vision-based robotic skins: a data-driven, multi-camera tactile sensor," in *2020 3rd IEEE International Conference on Soft Robotics (RoboSoft)*. IEEE, 2020, pp. 333–338.
- [11] N. Kuppuswamy, A. Alspach, A. Uttamchandani, S. Creasey, T. Ikeda, and R. Tedrake, "Soft-bubble grippers for robust and perceptive manipulation," in *2020 IEEE/RSJ International Conference on Intelligent Robots and Systems (IROS)*. IEEE, 2020, pp. 9917–9924.
- [12] W. Yuan, S. Dong, and E. H. Adelson, "Gelsight: High-resolution robot tactile sensors for estimating geometry and force," *Sensors*, vol. 17, no. 12, p. 2762, 2017.
- [13] S. Dong, W. Yuan, and E. H. Adelson, "Improved gelsight tactile sensor for measuring geometry and slip," in *2017 IEEE/RSJ International Conference on Intelligent Robots and Systems (IROS)*. IEEE, 2017, pp. 137–144.
- [14] E. Donlon, S. Dong, M. Liu, J. Li, E. Adelson, and A. Rodriguez, "Gelslim: A high-resolution, compact, robust, and calibrated tactile-sensing finger," in *2018 IEEE/RSJ International Conference on Intelligent Robots and Systems (IROS)*. IEEE, 2018, pp. 1927–1934.
- [15] I. Taylor, S. Dong, and A. Rodriguez, "Gelslim3. 0: High-resolution measurement of shape, force and slip in a compact tactile-sensing finger," *arXiv preprint arXiv:2103.12269*, 2021.
- [16] A. Padmanabha, F. Ebert, S. Tian, R. Calandra, C. Finn, and S. Levine, "Omniact: A multi-directional high-resolution touch sensor," in *2020 IEEE International Conference on Robotics and Automation (ICRA)*. IEEE, 2020, pp. 618–624.
- [17] M. Lambeta, P.-W. Chou, S. Tian, B. Yang, B. Maloon, V. R. Most, D. Stroud, R. Santos, A. Byagowi, G. Kammerer *et al.*, "Digit: A novel design for a low-cost compact high-resolution tactile sensor with application to in-hand manipulation," *IEEE Robotics and Automation Letters*, vol. 5, no. 3, pp. 3838–3845, 2020.
- [18] Q. Li, O. Kroemer, Z. Su, F. F. Veiga, M. Kaboli, and H. J. Ritter, "A review of tactile information: Perception and action through touch," *IEEE Transactions on Robotics*, vol. 36, no. 6, pp. 1619–1634, 2020.
- [19] Y. She, S. Wang, S. Dong, N. Sunil, A. Rodriguez, and E. Adelson, "Cable manipulation with a tactile-reactive gripper," *arXiv preprint arXiv:1910.02860*, 2019.
- [20] W. Yuan, R. Li, M. A. Srinivasan, and E. H. Adelson, "Measurement of shear and slip with a gelsight tactile sensor," in *2015 IEEE International Conference on Robotics and Automation (ICRA)*. IEEE, 2015, pp. 304–311.
- [21] L. Cramphorn, J. Lloyd, and N. F. Lepora, "Voronoi features for tactile sensing: Direct inference of pressure, shear, and contact locations," in *2018 IEEE International Conference on Robotics and Automation (ICRA)*. IEEE, 2018, pp. 2752–2757.
- [22] W. Yuan, S. Wang, S. Dong, and E. Adelson, "Connecting look and feel: Associating the visual and tactile properties of physical materials," in *Proceedings of the IEEE Conference on Computer Vision and Pattern Recognition*, 2017, pp. 5580–5588.
- [23] R. Li, R. Platt, W. Yuan, A. ten Pas, N. Roscup, M. A. Srinivasan, and E. Adelson, "Localization and manipulation of small parts using gelsight tactile sensing," in *2014 IEEE/RSJ International Conference on Intelligent Robots and Systems (IROS)*. IEEE, 2014, pp. 3988–3993.
- [24] M. Bauza, O. Canal, and A. Rodriguez, "Tactile mapping and localization from high-resolution tactile imprints," in *2019 International Conference on Robotics and Automation (ICRA)*. IEEE, 2019, pp. 3811–3817.
- [25] Y. Zhang, Z. Kan, Y. A. Tse, Y. Yang, and M. Y. Wang, "Fingervision tactile sensor design and slip detection using convolutional lstm network," *arXiv preprint arXiv:1810.02653*, 2018.
- [26] Y. Zhang, W. Yuan, Z. Kan, and M. Y. Wang, "Towards learning to detect and predict contact events on vision-based tactile sensors," in *Conference on Robot Learning*. PMLR, 2020, pp. 1395–1404.
- [27] G. Zhang, Y. Du, Y. Zhang, and M. Y. Wang, "A tactile sensing foot for single robot leg stabilization," in *2021 IEEE International Conference on Robotics and Automation (ICRA)*, 2021, pp. 14 076–14 082.

- [28] C. Pang, K. Mak, Y. Zhang, Y. Yang, Y. A. Tse, and M. Y. Wang, "Viko: An adaptive gecko gripper with vision-based tactile sensor," in *2021 IEEE International Conference on Robotics and Automation (ICRA)*, 2021, pp. 736–742.
- [29] G. Farnebäck, "Two-frame motion estimation based on polynomial expansion," in *Scandinavian conference on Image analysis*. Springer, 2003, pp. 363–370.
- [30] G. Bradski, "The OpenCV Library," *Dr. Dobb's Journal of Software Tools*, 2000.
- [31] K. He and J. Sun, "Fast guided filter," *arXiv preprint arXiv:1505.00996*, 2015.
- [32] Y. Zhang, Z. Kan, Y. Yang, Y. A. Tse, and M. Y. Wang, "Effective estimation of contact force and torque for vision-based tactile sensors with helmholtz–hodge decomposition," *IEEE Robotics and Automation Letters*, vol. 4, no. 4, pp. 4094–4101, 2019.
- [33] H. Bhatia, V. Pascucci, and P.-T. Bremer, "The natural helmholtz-hodge decomposition for open-boundary flow analysis," *IEEE transactions on visualization and computer graphics*, vol. 20, no. 11, pp. 1566–1578, 2014.